Thickness dependence of scattering cross-sections in quantitative scanning transmission electron microscopy

Thickness dependence of scattering cross-sections in quantitative scanning transmission electron microscopy

G. T. Martinez[a], K. H. W. van den Bos[a], M. Alania[a], P. D. Nellist[b], S. Van Aert[a]

[a] *Electron Microscopy for Materials Science (EMAT), University of Antwerp, Gronenborgerlaan 171, 2020 Antwerp, Belgium*
[b] *Department of Materials, Oxford University, Parks Road, Oxford OX1 3PH, United Kingdom*

Abstract

In quantitative scanning transmission electron microscopy (STEM), scattering cross-sections have been shown to be very sensitive to the number of atoms in a column and its composition. They correspond to the integrated intensity over the atomic column and they outperform other measures. As compared to atomic column peak intensities, which saturate at a given thickness, scattering cross-sections increase monotonically. A study of the electron wave propagation is presented to explain the sensitivity of the scattering cross-sections. Based on the multislice algorithm, we analyse the wave propagation inside the crystal and its link to the scattered signal for the different probe positions contained in the scattering cross-section for detector collection in the low-, middle- and high-angle regimes. The influence to the signal from scattering of neighbouring columns is also discussed.

Keywords:

ADF STEM, electron scattering, quantitative STEM, image simulation

1. Introduction

Quantitative scanning transmission electron microscopy (STEM) has become a widely used technique to retrieve structural information from a material under study. It generally refers to the analysis of images obtained using a scanning transmission electron microscope in which the electrons are usually collected using an annular detector, although detectors with different configurations are also becoming more widely available [1, 2, 3, 4, 5]. The choice of inner and outer collection angles of an annular detector allows one to collect electrons scattered over a specific angular range resulting in specific structural information of the sample. Electrons that scatter at high angles are related to the atomic number Z of the atoms they interact with, allowing so-called Z-contrast imaging [6, 7]. Other collection angle regimes enable imaging of light elements or strained samples [8, 9, 10]. In the annular dark field (ADF) regime, the signal is considered predominantly incoherent [11, 12], which facilitates the interpretation of the images due to the lack of contrast reversals. In this collection angle regime quantitative methods have been developed to analyse images. The proposed quantitative methodologies usually follow either an image simulation-based or a statistics-based approach. Image simulation-based methods depend on the direct comparison of experimental images with simulations [13, 14, 15, 16, 17, 18, 19]. The experimental images need to be normalised with respect to the incident beam [14, 16, 20]. In addition, image simulations need to be performed using models that describe the electron-sample interaction as accurately as possible [21, 22, 23, 24, 25, 26, 27]. Furthermore, the experimental conditions [28] as well as the detector's response [20, 29, 30, 31, 32, 19] need to be known

up to the measurable limits. On the other hand, statistics-based methods consider a statistical parameter estimation framework to extract quantitative information from STEM images [33, 34]. They make use of parametric models of which the unknown parameters are estimated by fitting the model to the experimental images using a criterion of goodness of fit. The quantitative information is then retrieved from these estimated model parameters and can be directly related to the chemical composition [34, 35] or number of atoms in an atomic column [36, 37], for example. When combined with tomography techniques, these methods allow the three-dimensional reconstruction of a material at the atomic level [38, 39, 40] without the need of image simulations. The tools of statistical experimental design can be used to find the optimal microscope settings to retrieve the information of interest [41, 42, 43, 44]. It has also been shown that a combination of statistics-based and image simulation-based methods leads to both accurate and precise structure parameters [20, 35, 36, 43, 45, 46].

Different measures have been used to quantify STEM images including peak intensities at the atomic column position or contrast variations [7, 31], the mean intensity of the material's unit cell [10, 16, 17, 30], the volume under a Gaussian function fitted at the atomic column position [35, 34, 36, 37] or the pixel integrated scattering cross-sections [18, 20, 47]. The latter two have been found to be equivalent and are referred to as the so-called scattering cross-section of an atomic column, which corresponds to the total amount of scattered electrons by a single atomic column. A detailed derivation of this measure can be found in [47].

De Backer et al. [44] showed that in order to precisely count the number

of atoms, the scattering cross-sections perform as well as when comparing images and simulations on a pixel by pixel basis. Furthermore, peak intensities, which correspond to the maximum intensity recorded at the atomic column position, have been found to provide less reliable results. The scattering cross-section has also been found to be robust to probe parameters in contrast to peak intensities [47, 48]. Previous experimental work has quantified Pt systems using scattering cross-sections [18, 20, 43, 46]. Therefore, we present an in-depth simulation study of a Pt system to investigate the sensitivity of scattering cross-sections with respect to thickness. In Figure 1 the increase of scattering cross-section (left blue vertical-axis) and peak intensity (right green vertical-axis) is shown as a function of sample thickness for a Pt crystal viewed along the [110] zone axis under high angle annular dark field (HAADF) conditions for a 21 mrad probe convergence angle (See Table 1). Scattering cross-section axis units are Megabarn ($1Mb = 10^{-22}m^2$) and for peak intensity, the axis is in fractional beam current. From this plot, it is clear that peak intensities saturate around ≈ 6 atoms, whereas the scattering cross-sections keep increasing with increasing thickness. Therefore, when trying to distinguish between e.g. 10 and 11 atoms, the peak intensity measure is not adequate since there is practically no variation between the corresponding intensity values. On the other hand, when using the scattering cross-section values, a clear difference is observed.

In this work, we explain the monotonically increase of scattering cross-sections for the number of atoms in a sample as shown in Figure 1. For this, we analyse how the probe propagates through the crystal and how this process contributes to the peak intensity and to the scattering cross-section

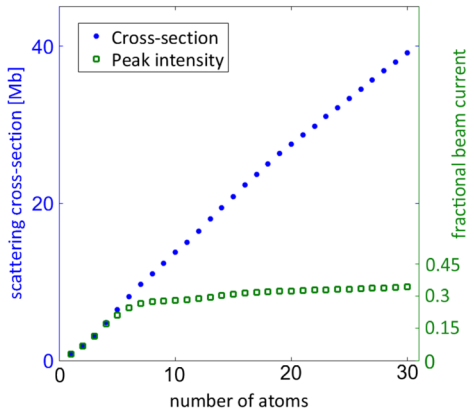

Figure 1: Scattering cross-section (left blue vertical-axis) and peak intensity (right green vertical-axis) as a function of sample thickness for Pt in [110] zone axis. ADF STEM detector collection angles ranging from 63 to 200 mrad for a 21 mrad probe convergence angle (See Table 1).

values. Consequently, a set of image simulations describing the wavefunction propagation through the crystal for different probe positions has been carried out by using the multislice algorithm [49, 50]. With the information these calculations provide, we are able to infer the origin of the detected signal and its contribution to the scattering cross-section value.

2. Background and methods

In order to characterise the atomic columns in 3D from a STEM image, one needs to use the image intensities that originate from conditions where the electron wavefunction is peaked at the atomic column. Therefore, a thorough understanding of the interaction between the electron wavefunction and the sample for each STEM probe position is needed. The multislice algorithm allows one to calculate the electron wavefunction $\psi(x, y)$ inside

the crystal as a function of depth. The modulus squared of the electron wavefunction $|\psi(x,y)|^2$ at a specific crystal thickness indicates the probability to find the electron at a certain point (x,y) in space [51, 52]. If the probability $|\psi(x,y)|^2$ is found to be high near the atomic column potential, it can be inferred that the scattering reaching the detector has its main origin from this site. Thus, by using this method, one can retrieve information about the interaction of the electron wave and the sample as well as its relationship to the detected signal.

In order to analyse the wave propagation of the electron through the crystal, $|\psi(x,y)|^2$ is calculated for each probe position (x_p, y_p) contributing to the scattering cross-section. This was carried out for different thicknesses of a Pt sample in [110] zone axis using the frozen lattice multislice approach using the STEMSim software [53]. The simulations were carried out for a crystal using two different probe convergence angles (21 and 31 mrad). To study the contribution of scattered intensity of neighbouring columns, simulations of an isolated column for the 21 mrad case were also carried out. Simulation details are presented in Table 1. In this work, the collection angle regimes are defined as: Low-Angle Annular Dark Field (LAADF), Middle-Angle Annular Dark Field (MAADF) and High-Angle Annular Dark Field (HAADF), which correspond to integrating the signal from 1, 2 or 3 times the convergence angle α as inner collection angle up to the outer collection angle, respectively. Other similar integration regimes have been suggested in [54].

Figure 2 a) shows a simulated Z-contrast image of Pt. A unit cell is selected to illustrate the analysis procedure followed in this work. From this

Table 1: Frozen lattice simulations settings

Acceleration voltage HT	300 kV
Defocus C_1	0 nm
Spherical aberration C_3	-142 nm
Convergence semi-angle α	21 mrad /31 mrad
Spatial incoherence of source FWHM	0.7 Å
LAADF inner collection angle	21 mrad /31 mrad
MAADF inner collection angle	42 mrad /62 mrad
HAADF inner collection angle	63 mrad /93 mrad
LAADF/MAADF/HAADF outer collection angle	200 mrad
Detector's response	homogeneous (ideal)
Zone axis	[110]
Supercell periodicity	9 x 9 unit cells
Supercell size	24.97 x 35.31 $Å^2$
Maximum specimen thickness	8.32 nm
Number of phonon configurations	20
Pixel size of simulated image	0.1394 Å
Pixel size to sample atomic potential	0.0293 Å

unit cell image, the pixel values corresponding to different probe positions have been coloured with respect to their distance to the atomic column position and are shown in Figure 2 b). As it can be observed, the dark red pixel (peak intensity) corresponds to the centre of the atomic column (labelled as **r0**). The nine light red pixels closest to the atomic column position correspond to a distance of $\approx$ 14 pm (labelled as **r1**). The next twelve orange pixels indicate the probe positions at $\approx$ 28 pm (labelled as **r2**) and so on. The labels in Figure 2 b) show the corresponding colours and distances for these probe positions (pixels). All these probe positions contribute to the scattering cross-section of the column, labelled as **XS**. We will use the term 'radial probe position' to refer to these probe positions. For example, radial probe position **r2** corresponds to the summed contribution of all the orange pixels (probe positions) depicted in Figure 2 b).

For the analysis of the wave propagation inside the crystal, the following procedure has been carried out. First, the modulus squared of the wavefunction $|\psi(x, y)|^2$ at probe position (x_p, y_p) for each of 20 phonon configurations has been averaged for each thickness. Next, the resulting probabilities of the corresponding probe positions that form each radial probe position have been summed. For example, for radial probe position **r2**, the probabilities corresponding to the probe positions depicted in orange in Figure 2 b) have been summed. Finally, the summed probability of each radial probe position has been rotationally averaged using the atomic column position in the centre. In this way, the interaction between the electron wave and the atomic column can be identified with respect to the atomic column position as origin. In order to study the contributions from the neighbouring columns, the

summed probabilities have been rotationally averaged using the coordinates of the closest neighbouring column as a reference.

3. Results and discussion

3.1. Analysis of the wavefunction propagation for different probe positions

The wavefunction obtained from the multislice algorithm for the two convergence angles up to 30 Pt atoms has been used to analyse its propagation through the crystal. Figures 3 and 4 show the rotationally averaged variation of $|\psi(x, y)|^2$ with respect to the number of atoms in depth (vertical-axis) and the distance from the atomic column (horizontal-axis) for the different radial probe positions shown in Figure 2 and the total scattering cross-section **XS** for convergence angle 21 mrad and 31 mrad respectively. The electron wavefunction propagation through the crystal can be observed in these plots.

For the 21 mrad probe convergence angle example, the wavefunction at the atomic column position **r0** clearly excites the atomic column up to ≈ 6 atoms and then disperses. For off-column probe positions, the electron interacts with the atomic column at higher thickness. For example, for probe positions close to the atomic column, that is **r1** (≈ 14 pm) to **r3** (≈ 42 pm), the wavefunction mainly excites the atomic column at a depth of ≈ 3 to 12 atoms. The probe positioned at **r4** (≈ 56 pm) and **r5** (≈ 70 pm) contains contributions at a depth of ≈ 10 to 20 atoms. Even for radial probe positions further away, that is **r6** (≈ 84 pm) to **r8** (≈ 112-126 pm), the wavefunction propagates to the atomic column position for depths up to 30 atoms. One should note that the colour scale-bar of each plot of Figure 3 and 4 is different in order to show clearly the excitation of the atomic column. These figures

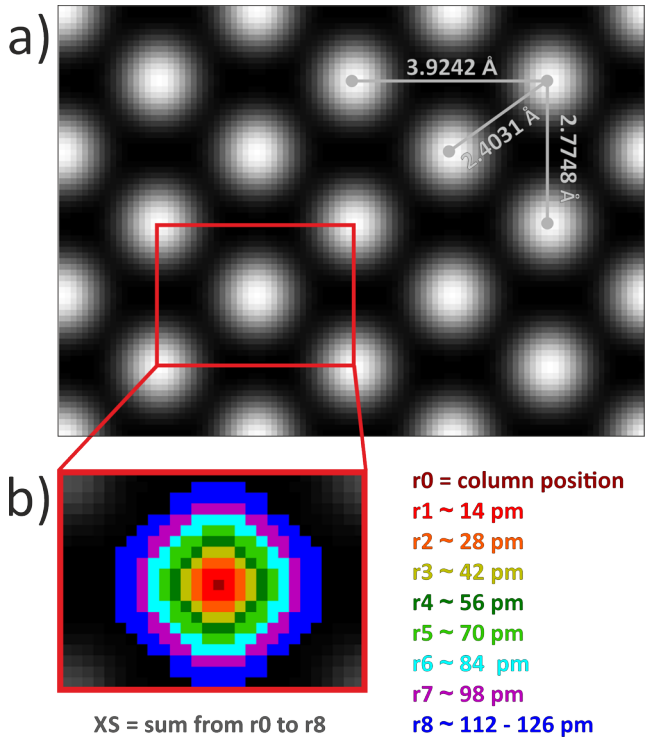

Figure 2: a) Simulated image of Pt in [110] zone axis using simulation settings described in Table 1 for the HAADF case using a 21 mrad probe convergence angle. Depicted distances show the separation between columns for this material. b) Colour-edited simulated image of Pt and colour labels with their corresponding distances from the atomic column position. The label **XS** refers to the scattering cross-section, which is the summation over all radial probe positions.

qualitatively indicate which part of the atomic column is excited by the electron probe. In this manner, one can infer from which part of the crystal the contributions to the scattering cross-section originate.

When comparing with the 31 mrad probe convergence angle case, we can observe that the wavefunction excites the atomic column at different depths depending on the radial probe position in a more localised manner. For example, when comparing the probabilities at probe position **r4** ($\approx$ 56 pm) from Figures 3 and 4, we can observe that for the 31 mrad case, the column is excited from $\approx$ 7 to 12 atoms. In contrast, for the 21 mrad example, the excitation of the atomic column ranges from $\approx$ 6 to 16 atoms. This observation is in agreement with the fact that for a higher convergence angle, the depth resolution increases [55, 56].

An important observation is that the excitation of the column occurs at depths that are related to the broadening of the probe when considering a free propagation of the wave. This propagation of the electron wave in vacuum is illustrated by the dashed lines in Figure 3 and 4. Therefore, the interaction at different depths of the column for each radial probe position depends on the convergence angle of the probe.

As it will be shown in the next section, the increase of scattering cross-section as a function of thickness as shown in Figure 1 can be explained because of the excitation of the atomic column at larger depth when the probe is located away from the column position. Moreover, the saturation of the peak intensity results from the reduced interaction of the wavefunction with the atomic column at the corresponding depth.

Another aspect to consider in this analysis is how the wave interacts with

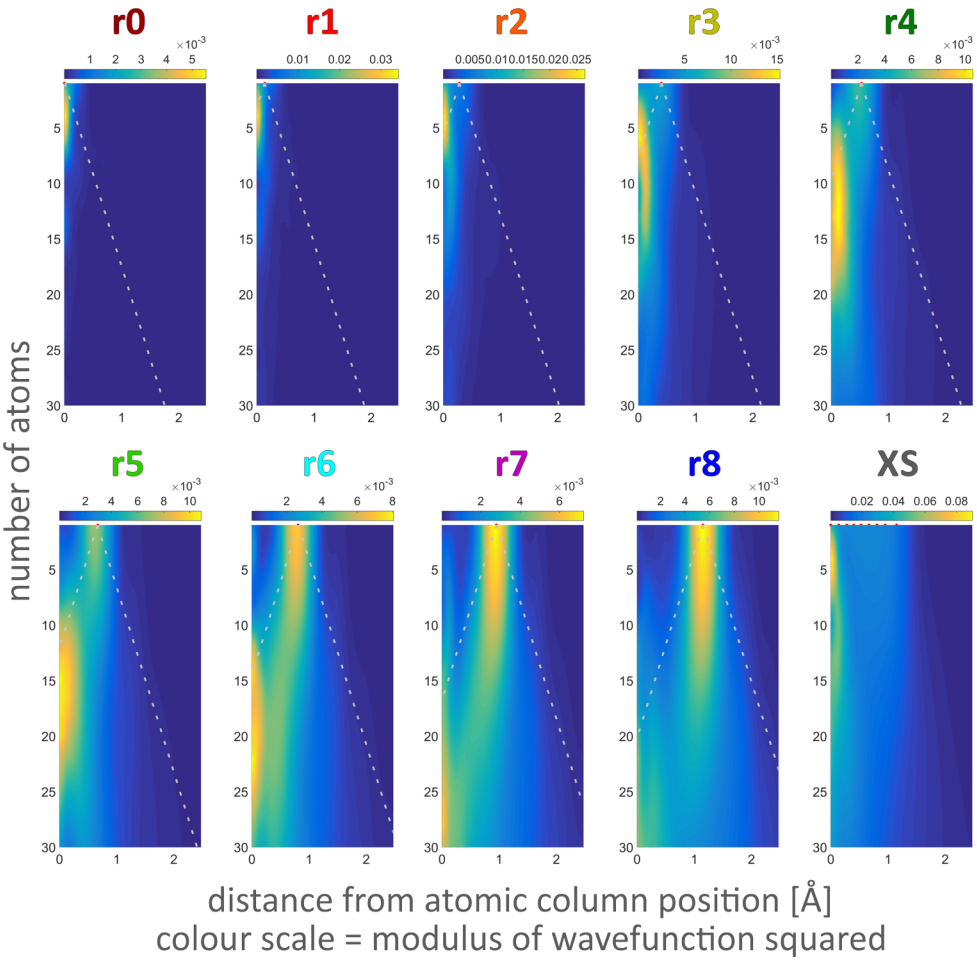

Figure 3: Rotationally averaged variation of $|\psi(x,y)|^2$ with respect to number of atoms and distance from the atomic column for the different probe positions depicted in Figure 2 and for the scattering cross-section **XS** for a 21 mrad probe convergence angle. Dashed lines indicate the broadening of the probe as if it would propagate in vacuum.

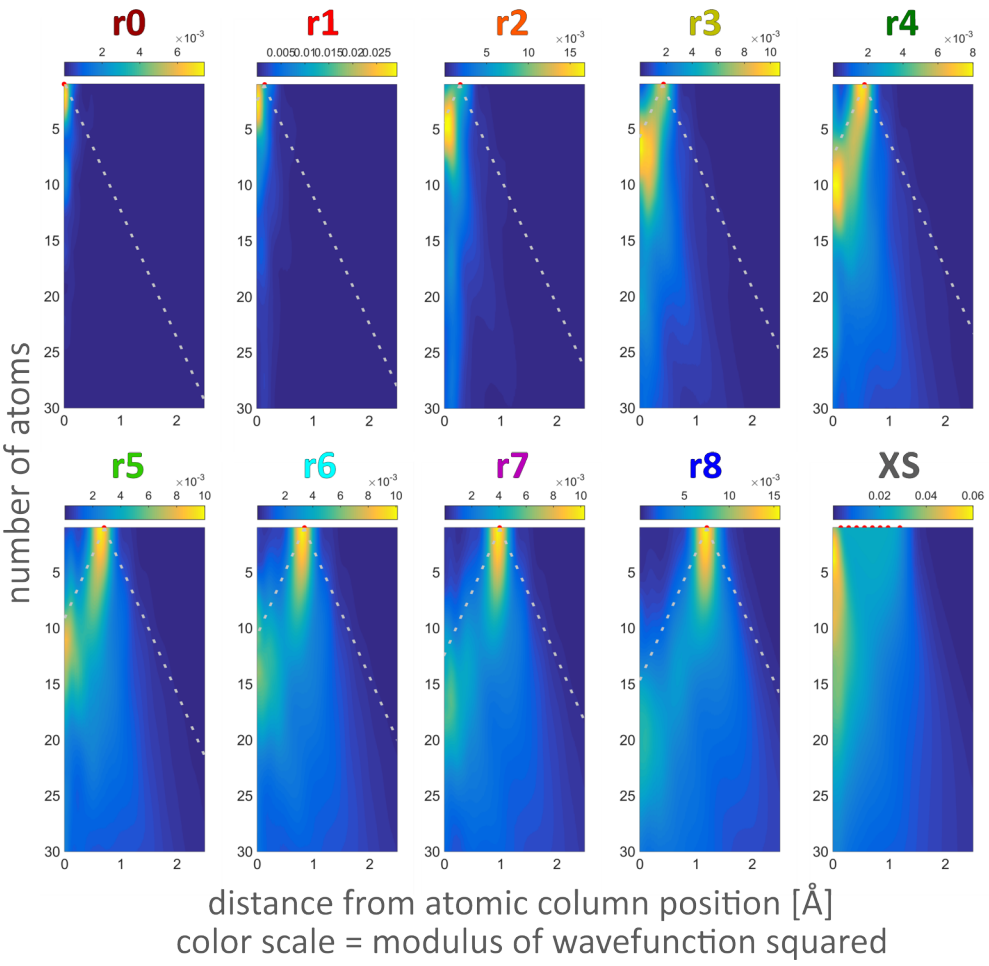

Figure 4: Rotationally averaged variation of $|\psi(x, y)|^2$ with respect to number of atoms and distance from the atomic column for the different probe positions depicted in Figure 2 and for the scattering cross-section **XS** for a 31 mrad probe convergence angle. Dashed lines indicate the broadening of the probe as if it would propagate in vacuum.

the neighbouring columns. This interaction is related to the dispersion of the wave as it propagates inside the crystal. The dispersion increases the probability to interact with neighbouring atomic column potentials, which can also scatter electrons towards the detector. To understand this, the same procedure of rotationally averaging $|\psi(x,y)|^2$ was performed using the atomic column position of the closest neighbouring column as origin. Figure 5 shows the rotationally averaged variation of $|\psi(x,y)|^2$ with respect to the number of atoms (vertical-axis) and the distance from the neighbouring atomic column (horizontal-axis) for the different probe positions used in this analysis for the 21 mrad probe convergence angle example. Colour scale-bars for each plot have been adapted to show features more clearly. In general, one can observe an interaction of the electron wave with the neighbouring columns for depths beyond $\approx$ 20 atoms. The probability of interaction with the neighbouring column increases as the wave propagates inside the crystal and as the probe is located closer to the neighbouring atomic column. When comparing the colour scale-bar of Figures 3 and 5, it is clear that the effect of neighbouring columns is at least an order of magnitude smaller. This indicates that the probability of the electron wave interacting with the neighbouring columns is smaller than the interaction of the electron wave with the main atomic column. How much of this interaction is converted into detected signal and from which thickness this becomes significant is discussed in the next section.

3.2. Contribution of different probe positions to the scattering cross-section

The analysis presented in the previous section allows us to understand the electron-sample interaction at the sample plane for the different probe positions that form the scattering cross-section. However, the images are

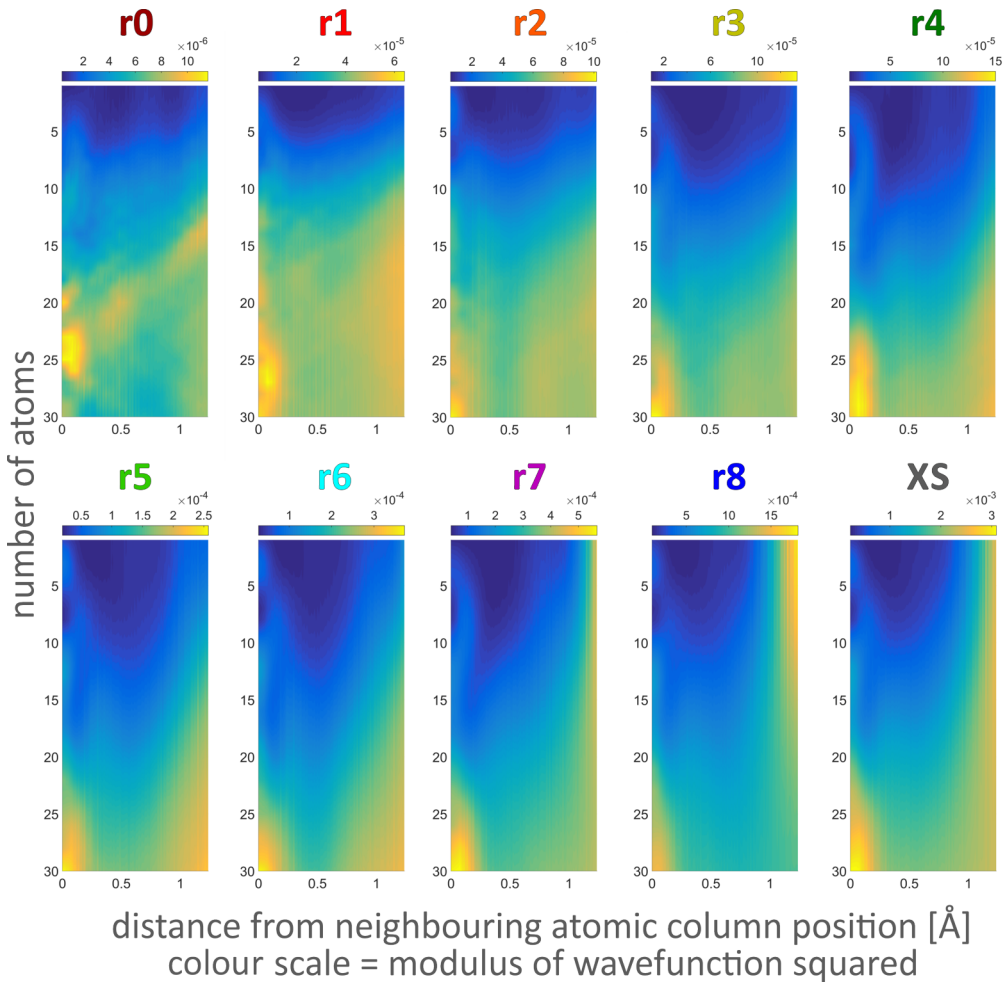

Figure 5: Rotationally averaged variation of $|\psi(x, y)|^2$ with respect to number of atoms and distance from the neighbouring atomic column for the different probe positions depicted in Figure 2.

formed by integrating the scattered signal at the detector plane. The next analysis investigates the contribution of each radial probe position to the scattering cross-section value in order to understand their relative importance. As described in Section 2, we consider three collection regimes of the detector: LAADF, MAADF and HAADF and the analysis is performed for the 21 mrad probe convergence angle simulation set.

The intensity contribution of the radial probe positions to the scattering cross-section value for the different regimes is shown in Figure 6. We can observe in these plots that for radial probe position **r0**, that is, the peak intensity at the atomic column position, the contribution to the scattering cross-section is 5% or less for any of the integration collection angles. This probe position has the highest value in comparison to all other probe positions. However, since the scattering cross-section value is the sum of many probe positions, the peak intensity value originates from only one probe position and thus adds up only once.

Next, it is found that for small sample depths ($\approx$ 1 to 10 atoms), the main contribution in MAADF and HAADF is predominantly given by the radial probe position close to the atomic column ($\approx$ 14 to 42 pm). Indeed, these pixel values in the image have a very similar value close to the peak intensity at atomic column position but since there are more probe positions adding to the cross-section value, their contribution is higher. In contrast, for LAADF, the contributions of the different radial probe positions for small thicknesses does not show a specific trend. This is related to the strong presence of elastic scattering observed as channelling oscillations.

For large sample depths ($\approx$ 20 to 30 atoms), it is observed that the con-

tributions of radial probe positions further from the atomic column, that is, **r6** ($\approx$ 84 pm) to **r8** ($\approx$ 112-126 pm), is predominant regardless of the integration regime. This is explained by considering that the atomic column is strongly excited for these probe positions, as it was discussed in the previous section, depending on the probe convergence angle used. There is small interaction for probe positions close to the atomic column at large depths, since the electrons have already been strongly scattered.

In order to study the contribution of the neighbouring columns, two sets of simulations are analysed. One set is carried out for the full crystal structure and the other considers an isolated atomic column. The difference between the signals of both simulations can be attributed to the interaction of the probe with the neighbouring columns present in the crystal. Figure 7 shows the scattered intensity as a function of the number of atoms in the column for each radial probe position for the different detector integration regimes for both crystal and isolated atom simulations. In the LAADF signal, one can observe the channelling oscillations due to the elastic interaction of the electron wave with the atomic column potential. For probe positions **r0** to **r5**, these channelling oscillations are clearly identified. For these probe positions, the difference between the signal of the full crystal and the isolated atomic column simulations becomes noticeable for large sample thickness ($\approx$ 20 to 30 atoms) whereas for probe positions **r6** to **r8**, these discrepancies are also present at smaller depths ($\approx$ 2 to 10 atoms). For MAADF and HAADF, the scattered signal increases monotonically with a small difference between the full crystal simulation and the isolated atomic column for probe positions close to the column ($\approx$ 14 to 70 pm) but a higher difference for

probe positions far from it.

The overall contribution of the neighbouring columns to the scattering cross-section can be observed in Figure 8, in which the total scattered intensity in the cross-section area is plotted with respect to the number of atoms for the discussed integration regimes. From this plot, we can conclude that the contribution of the neighbouring columns to the scattering cross-section is predominantly found at large sample depths ($\approx$ 20 to 30 atoms), due to the electron wave dispersion inside the crystal.

4. Conclusions

In this work, an analysis of the propagation of the electron wave inside a Pt [110] crystal has been carried out in order to understand why scattering cross-sections provide a more complete measure when compared with peak intensities. It is observed that for the peak intensity, the atomic column is excited up to a certain number of atoms whereas for the cross-section it is excited deeper inside the column by the different probe positions. This explains why the scattering cross-section shows an increasing behaviour as compared to the peak intensity, which reaches a saturation plateau at a certain thickness. Since we integrate over probe positions to obtain the cross-section, information from different depths is included in this measure. The results depend on the convergence angle and the broadening of the probe. Furthermore, contributions from neighbouring columns become important at higher sample thicknesses because of the wave dispersion inside the crystal. Depending on the detector collection angles, the contribution to the scattering cross-section of each radial probe position is different. For LAADF, the

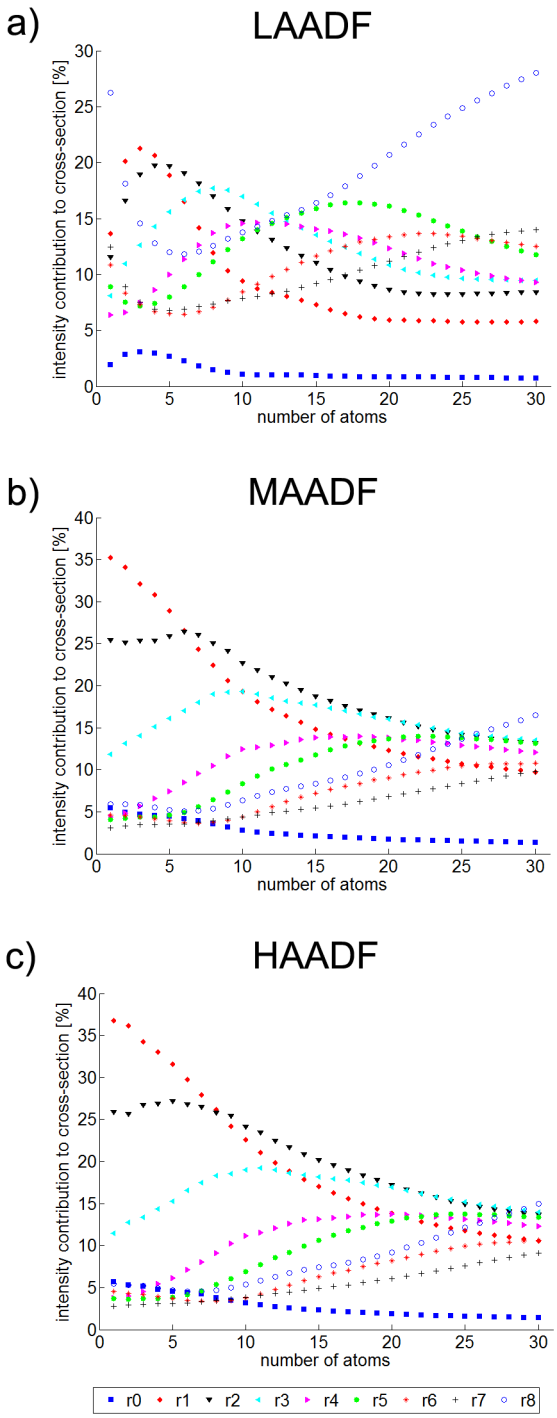

Figure 6: Intensity contributions in percentage to the scattering cross-section value for a) LAADF, b) MAADF and c) HAADF. Simulations considered a 21 mrad probe convergence angle.

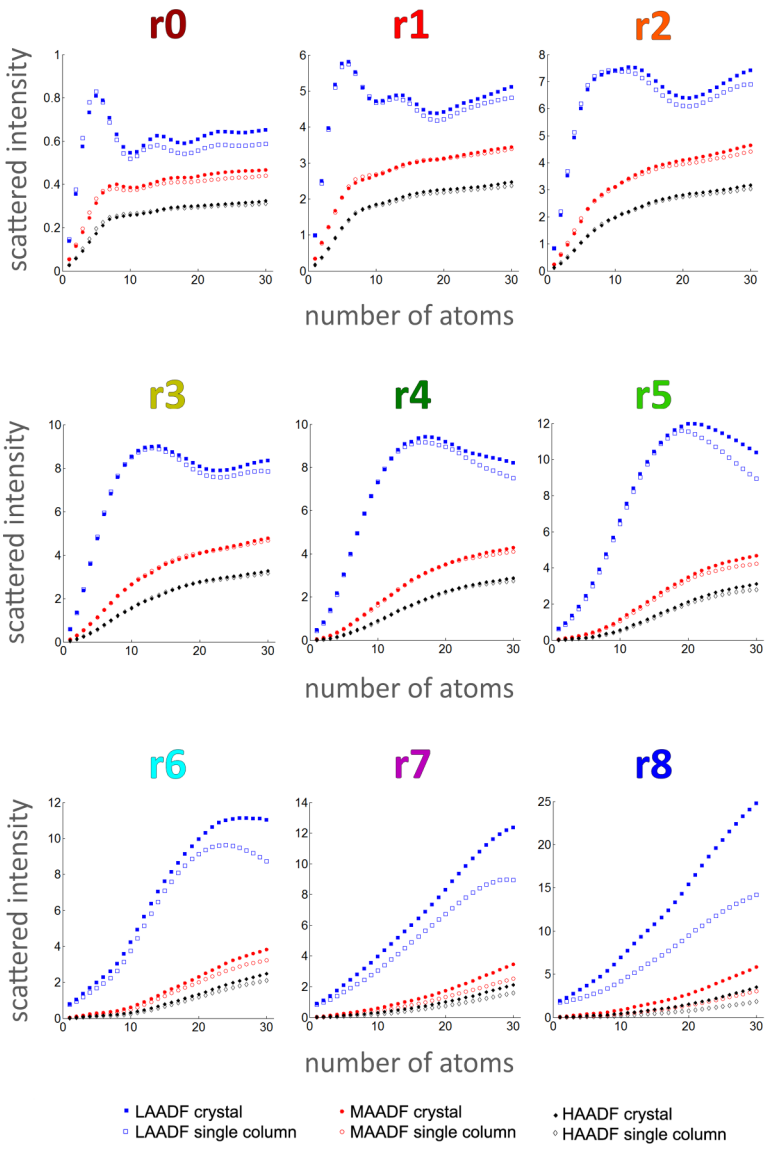

Figure 7: Scattered intensity with respect to number of atoms for radial probe positions **r0** to **r8** for LAADF, MAADF and HAADF detector collection angle regimes. Simulations considered a 21 mrad probe convergence angle for a crystal and an isolated atomic column.

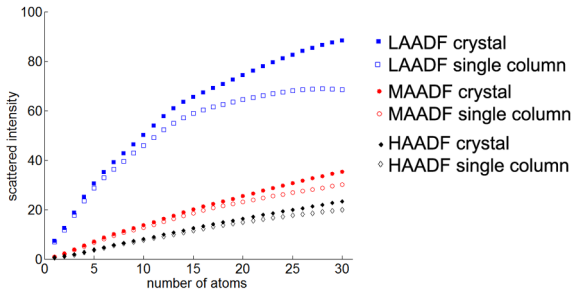

Figure 8: Scattered intensity integrated in the cross-section area with respect to number of atoms for LAADF, MAADF and HAADF detector collection angle regimes. Simulations considered a 21 mrad probe convergence angle for a crystal and an isolated atomic column.

oscillations due to channeling are identified. For the case of MAADF and HAADF, the behaviour of the cross-section increases monotonically and the contribution from probe positions near the column is predominant for small sample depths. For all collection regimes, the contribution of neighbouring columns at large sample thickness for probe positions far from the atomic column becomes important.

Acknowledgements

The authors acknowledge financial support from the Research Foundation Flanders (FWO, Belgium) through project fundings (G.0374.13N, G.0369.15N, G.0368.15N and WO.010.16N) and a PhD grant to K.H.W.v.d.B. The research leading to these results has received funding from the European Union 7th Framework Programme [FP7/2007-2013] under Grant agreement no.312483 (ESTEEM2). The authors are grateful to A. Rosenauer for providing access to the StemSim software.

[1] N. Shibata, Y. Kohno, S. D. Findlay, H. Sawada, Y. Kondo, Y. Ikuhara, New area detector for atomic-resolution scanning transmission electron microscopy, Journal of Electron Microscopy 59 (2010) 473 – 479.

[2] N. Shibata, S. D. Findlay, Y. Kohno, H. Sawada, Y. Kondo, Y. Ikuhara, Differential phase-contrast microscopy at atomic resolution, Nature Physics 8 (2012) 611 – 615.

[3] M. Lohr, R. Schregle, M. Jetter, C. Wächter, T. Wunderer, F. Scholz, J. Zweck, Differential phase contrast 2.0 - Opening new "fields" for an established technique, Ultramicroscopy 117 (2012) 7 – 14.

[4] T. J. Pennycook, A. R. Lupini, H. Yang, M. F. Murfitt, L. Jones, P. D. Nellist, Efficient phase contrast imaging in STEM using a pixelated detector. Part 1: Experimental demonstration at atomic resolution , Ultramicroscopy 151 (2015) 160 – 167, special Issue: 80th Birthday of Harald Rose; PICO 2015 Third Conference on Frontiers of Aberration Corrected Electron Microscopy.

[5] H. Yang, T. J. Pennycook, P. D. Nellist, Efficient phase contrast imaging in STEM using a pixelated detector. Part II: Optimisation of imaging conditions , Ultramicroscopy 151 (2015) 232 – 239, special Issue: 80th Birthday of Harald Rose; PICO 2015 Third Conference on Frontiers of Aberration Corrected Electron Microscopy.

[6] S. J. Pennycook, D. E. Jesson, High-resolution Z-contrast imaging of crystals, Ultramicroscopy 37 (1991) 14–38.

[7] D. O. Klenov, S. Stemmer, Contributions to the contrast in experimental high-angle annular dark-field images, Ultramicroscopy 106 (2006) 889–901.

[8] Y. Oshima, H. Sawada, F. Hosokawa, E. Okunishi, T. Kaneyama, Y. Kondo, S. Niitaka, H. Takagi, Y. Tanishiro, K. Takayanagi, Direct imaging of lithium atoms in LiV_2O_4 by spherical aberration-corrected electron microscopy, Journal of Electron Microscopy 59 (6) (2010) 457–461.

[9] S. D. Findlay, N. Shibata, H. Sawada, E. Okunishi, Y. Kondo, Y. Ikuhara, Dynamics of annular bright field imaging in scanning transmission electron microscopy, Ultramicroscopy 110 (7) (2010) 903 – 923.

[10] T. Grieb, K. Mueller, R. Fritz, M. Schowalter, N. Neugebohrn, N. Knaub, K. Volz, A. Rosenauer, Determination of the chemical composition of GaNAs using STEM HAADF imaging and STEM strain state analysis, Ultramicroscopy 117 (2012) 15–23.

[11] P. Hartel, H. Rose, C. Dinges, Conditions and reasons for incoherent imaging in STEM, Ultramicroscopy 63 (1996) 93–114.

[12] P. D. Nellist, S. J. Pennycook, Incoherent imaging using dynamically scattered coherent electrons, Ultramicroscopy 78 (1999) 111 – 124.

[13] J. M. LeBeau, S. D. Findlay, L. J. Allen, S. Stemmer, Quantitative Atomic Resolution Scanning Transmission Electron Microscopy, Physical Review Letters 100 (2008) 206101.

[14] J. M. LeBeau, S. Stemmer, Experimental quantification of annular dark-field images in scanning transmission electron microscopy, Ultramicroscopy 108 (2008) 1653–1658.

[15] J. M. LeBeau, S. D. Findlay, X. Wang, A. J. Jacobson, L. J. Allen, S. Stemmer, High-angle scattering of fast electrons from crystals containing heavy elements: Simulation and experiment, Physical Review B 79 (2009) 214110.

[16] A. Rosenauer, K. Gries, K. Mueller, A. Pretorious, M. Schowalter, A. Avramescu, K. Engl, S. Lutgen, Measurement of specimen thickness and composition in AlxGa1-xN/GaN using high-angle annular dark field images, Ultramicroscopy 109 (2009) 1171–1182.

[17] A. Rosenauer, T. Mehrtens, K. Mueller, K. Gries, M. Schowalter, P. Satyam, S. Bley, C. Tessarek, D. Hommel, K. Sebald, M. Seyfried, J. Gutowski, A. Avramescu, K. Engl, S. Lutgen, Composition mapping in InGaN by scanning transmission electron microscopy, Ultramicroscopy 111 (2011) 1316–1327.

[18] L. Jones, K. E. MacArthur, V. T. Fauske, A. T. J. van Helvoort, P. D. Nellist, Rapid Estimation of Catalyst Nanoparticle Morphology and Atomic-Coordination by High-Resolution Z-Contrast Electron Microscopy, Nano Letters 14 (11) (2014) 6336–6341.

[19] R. Ishikawa, A. R. Lupini, S. D. Findlay, S. J. Pennycook, Quantitative Annular Dark Field Electron Microscopy Using Single Elec-

tron Signals, Microscopy and Microanalysis 20 (1) (2014) 99110, doi: 10.1017/S1431927613013664.

[20] G. T. Martinez, L. Jones, A. De Backer, A. Béché, J. Verbeeck, S. Van Aert, P. D. Nellist, Quantitative STEM normalisation: The importance of the electron flux , Ultramicroscopy 159, Part 1 (2015) 46 – 58.

[21] R. F. Loane, P. Xu, J. Silcox, Thermal vibrations in convergent-beam electron diffraction, Acta Crystallographica Section A 47 (3) (1991) 267–278.

[22] D. A. Muller, B. Edwards, E. Kirkland, J. Silcox, Simulation of thermal diffuse scattering including a detailed phonon dispersion curve, Ultramicroscopy 86 (2001) 371–380.

[23] K. Ishizuka, A practical approach for STEM image simulation based on the FFT multislice method, Ultramicroscopy 90 (2002) 71–83.

[24] L. J. Allen, S. D. Findlay, M. P. Oxley, C. J. Rossouw, Lattice-resolution contrast from a focused coherent electron probe. Part I, Ultramicroscopy 96 (2003) 47–63.

[25] S. D. Findlay, L. J. Allen, M. P. Oxley, C. J. Rossouw, Lattice-resolution contrast from a focused coherent electron probe. Part II, Ultramicroscopy 96 (2003) 65–81.

[26] A. Rosenauer, M. Schowalter, J. Titantah, D. Lamoen, An emission-potential multislice approximation to simulate thermal diffuse scattering

in high-resolution transmision electron microscopy, Ultramicroscopy 108 (2008) 1504–1513.

[27] I. Lobato, D. Van Dyck, An accurate parametrisation for the scattering factors, electron densities and electrostatic potentials for neutral atoms that obey all physical constrains, Acta Crystallographica A 70 (2014) 636 – 649.

[28] C. Dwyer, C. Maunders, C. L. Zheng, M. Weyland, P. C. Tiemeijer, J. Etheridge, Sub-0.1 nm-resolution quantitative scanning transmission electron microscopy without adjustable parameters, Applied Physics Letters 100 (19) (2012) 191915.

[29] V. Grillo, An advanced study of the response of ADF detector, Journal of Physics: Conference Series 326 (1) (2011) 012036.

[30] T. Mehrtens, M. Schowalter, D. Tytko, P. Choi, D. Raabe, L. Hoffmann, H. Jönen, U. Rossow, A. Hangleiter, A. Rosenauer, Measurement of the indium concentration in high indium content InGaN layers by scanning transmission electron microscopy and atom probe tomography, Applied Physics Letters 102 (13) (2013) 132112.

[31] S. D. Findlay, J. M. LeBeau, Detector non-uniformity in scanning transmission electron microscopy, Ultramicroscopy 124 (2013) 52–60.

[32] K. E. MacArthur, L. Jones, P. Nellist, How Flat is Your Detector? Non-Uniform Annular Detector Sensitivity in STEM Quantification, Journal of Physics: Conference Series 522 (2014) 012018.

[33] S. Van Aert, W. Van den Broek, P. Goos, D. Van Dyck, Model-based electron microscopy: From images toward precise numbers for unknown structure parameters, Micron 43 (2012) 509–515.

[34] S. Van Aert, J. Verbeeck, R. Erni, S. Bals, M. Luysberg, D. Van Dyck, G. Van Tendeloo, Quantitative atomic resolution mapping using high-angle annular dark field scanning transmission electron microscopy, Ultramicroscopy 109 (2009) 1236–1244.

[35] G. T. Martinez, A. Rosenauer, A. De Backer, J. Verbeeck, S. Van Aert, Quantitative composition determination at the atomic level using model-based high-angle annular dark field scanning transmission electron microscopy, Ultramicroscopy 137 (2014) 12–19.

[36] S. Van Aert, A. De Backer, G. T. Martinez, B. Goris, S. Bals, G. Van Tendeloo, A. Rosenauer, Procedure to count atoms with trustworthy single-atom sensitivity, Physical Review B 87 (2013) 064107.

[37] A. De Backer, G. T. Martinez, A. Rosenauer, S. Van Aert, Atom counting in HAADF STEM using a statistical model-based approach: Methodology, possibilities, and inherent limitations, Ultramicroscopy 134 (2013) 23–33.

[38] S. Van Aert, K. J. Batenburg, M. D. Rossel, R. Erni, G. Van Tendeloo, Three-dimensional atomic imaging of crystalline nanoparticles, Nature 470 (2011) 374–377.

[39] S. Bals, M. Casavola, M. A. Van Huis, S. Van Aert, K. J. Batenburg, G. Van Tendeloo, D. Vanmaekelbergh, Three-Dimensional Atomic Imag-

ing of Colloidal Core-Shell Nanocrystals, NanoLetters 11 (2011) 3420–3424.

[40] A. De Backer, L. Jones, I. Lobato, T. Altantzis, B. Goris, P. D. Nellist, S. Bals, S. Van Aert, Three-dimensional atomic models from a single projection using Z-contrast imaging: verification by electron tomography and opportunities, Nanoscale 9 (2017) 8791–8798.

[41] S. Van Aert, A. den Dekker, D. Van Dyck, A. van den Bos, Optimal experimental design of STEM measurement of atom column positions, Ultramicroscopy 90 (2002) 273–289.

[42] J. Gonnissen, A. De Backer, A. J. den Dekker, G. T. Martinez, A. Rosenauer, J. Sijbers, S. Van Aert, Optimal experimental design for the detection of light atoms from high-resolution scanning transmission electron microscopy images, Applied Physics Letters (2014) 063116.

[43] A. De Backer, G. T. Martinez, K. E. MacArthur, L. Jones, A. Béché, P. D. Nellist, S. Van Aert, Dose limited reliability of quantitative annular dark field scanning transmission electron microscopy for nano-particle atom-counting, Ultramicroscopy 151 (0) (2015) 56 – 61, ISSN 0304-3991, doi:http://dx.doi.org/10.1016/j.ultramic.2014.11.028, special Issue: 80th Birthday of Harald Rose; PICO 2015 Third Conference on Frontiers of Aberration Corrected Electron Microscopy.

[44] A. De Backer, A. De wael, J. Gonnissen, S. Van Aert, Optimal experimental design for nano-particle atom-counting from high-resolution STEM images, Ultramicroscopy 151 (0) (2015) 46 – 55, ISSN 0304-

3991, doi:http://dx.doi.org/10.1016/j.ultramic.2014.10.015, special Issue: 80th Birthday of Harald Rose; PICO 2015 Third Conference on Frontiers of Aberration Corrected Electron Microscopy.

[45] A. M. Varambhia, L. Jones, A. De Backer, V. T. Fauske, S. Van Aert, D. Ozkaya, P. D. Nellist, Quantifying a Heterogeneous Ru Catalyst on Carbon Black Using ADF STEM, Particle and Particle Systems Characterization 33 (7) (2016) 438–444, ISSN 1521-4117, doi: 10.1002/ppsc.201600067.

[46] A. De wael, A. De Backer, L. Jones, P. D. Nellist, S. Van Aert, Hybrid statistics-simulations based method for atom-counting from ADF STEM images, Ultramicroscopy 177 (Supplement C) (2017) 69 – 77, ISSN 0304-3991.

[47] H. E, K. E. MacArthur, T. J. Pennycook, E. Okunishi, A. J. D'Alfonso, N. R. Lugg, L. J. Allen, P. D. Nellist, Probe integrated scattering cross sections in the analysis of atomic resolution HAADF STEM images, Ultramicroscopy 133 (0) (2013) 109 – 119.

[48] G. T. Martinez, A. De Backer, A. Rosenauer, J. Verbeeck, S. Van Aert, The effect of probe inaccuracies on the quantitative model-based analysis of high angle annular dark field scanning transmission electron microscopy images, Micron (2013) 57–63doi: http://dx.doi.org/10.1016/j.micron.2013.12.009.

[49] J. M. Cowley, A. F. Moodie, The scattering of electrons by atoms and crystals. I. A new theoretical approach, Acta Cryst. 10 (1957) 609–619.

[50] E. J. Kirkland, Advanced Computing in Electron Microscopy, Plenum Press, 1998.

[51] M. Born, Zur Quantenmechanik der Stoßvorgänge, Zeitschrift für Physik 37 (12) (1926) 863–867.

[52] H. Stapp, The Copenhagen Interpretation, American Journal of Physics 40 (1972) 1098–1116.

[53] A. Rosenauer, M. Schowalter, STEMSIM-a new software tool for simulation of STEM HAADF Z-contrast imaging, Springer Proceedings in Physics 120 (2007) 169–172.

[54] R. Hovden, D. A. Muller, Efficient elastic imaging of single atoms on ultrathin supports in a scanning transmission electron microscope, Ultramicroscopy 123 (2012) 59 – 65, albert Victor Crewe Memorial Issue.

[55] G. Behan, E. C. Cosgriff, A. I. Kirkland, P. D. Nellist, Three-dimensional imaging by optical sectioning in the aberration-corrected scanning transmission electron microscope 367 (1903) (2009) 3825–3844.

[56] R. Ishikawa, A. R. Lupini, Y. Hinuma, S. J. Pennycook, Large-angle illumination STEM: Toward three-dimensional atom-by-atom imaging, Ultramicroscopy 151 (2015) 122 – 129, ISSN 0304-3991, special Issue: 80th Birthday of Harald Rose; PICO 2015 Third Conference on Frontiers of Aberration Corrected Electron Microscopy.